AFM-IR nanospectroscopy of nanoglobule-like particles in Ryugu samples returned by the Hayabusa2 mission

Jérémie Mathurin, Laure Bejach, Emmanuel Dartois, Cécile Engrand, Alexandre Dazzi, Ariane Deniset-Besseau, Jean Duprat, Yoko Kebukawa, Hikaru Yabuta, Lydie Bonal, et al.

A&A, 684, A198 (2024)
https://doi.org/10.1051/0004-6361/202347435

Astronomy & Astrophysics

AFM-IR nanospectroscopy of nanoglobule-like particles in Ryugu samples returned by the Hayabusa2 mission

Jérémie Mathurin[1], Laure Bejach[2], Emmanuel Dartois[3], Cécile Engrand[2], Alexandre Dazzi[1], Ariane Deniset-Besseau[1], Jean Duprat[4], Yoko Kebukawa[5], Hikaru Yabuta[6], Lydie Bonal[7], Eric Quirico[7], Christophe Sandt[8], Ferenc Borondics[8], Jens Barosch[9], Pierre Beck[7], George D. Cody[9], Brad T. De Gregorio[10], Minako Hashiguchi[11], David A. L. Kilcoyne[12], Mutsumi Komatsu[13,14], Zita Martins[15], Megumi Matsumoto[16], Gilles Montagnac[17], Smail Mostefaoui[4], Larry R. Nittler[9], Takuji Ohigashi[18], Taiga Okumura[19], Van T. H. Phan[7], Laurent Remusat[4], Scott Sandford[20], Miho Shigenaka[6], Rhonda Stroud[21], Hiroki Suga[22], Yoshio Takahashi[19,23], Yasuo Takeichi[23], Yusuke Tamenori[24], Maximilien Verdier-Paoletti[4], Shohei Yamashita[23], Tomoki Nakamura[16], Tomoyo Morita[16], Mizuha Kikuiri[16], Kana Amano[16], Eiichi Kagawa[16], Takaaki Noguchi[25], Hiroshi Naraoka[26], Ryuji Okazaki[26], Kanako Sakamoto[27], Hisayoshi Yurimoto[28,29], Masanao Abe[27], Kanami Kamide[20], Akiko Miyazaki[27], Aiko Nakato[27], Satoru Nakazawa[27], Masahiro Nishimura[27], Tatsuaki Okada[27], Takanao Saiki[27], Shogo Tachibana[19,27], Satoshi Tanaka[27], Fuyuto Terui[30], Yuichi Tsuda[27], Tomohiro Usui[27], Sei-ichiro Watanabe[31], Toru Yada[27], Kasumi Yogata[27], and Makoto Yoshikawa[27]

(Affiliations can be found after the references)

Received 11 July 2023 / Accepted 18 January 2024

ABSTRACT

Context. The JAXA Hayabusa2 mission returned well-preserved samples collected from the carbonaceous asteroid Ryugu, providing unique non-terrestrially weathered samples from a known parent body.

Aims. This work aims to provide a better understanding of the formation and evolution of primitive asteroidal matter by studying the fine scale association of organic matter and minerals in Ryugu samples. We characterized the samples by IR nanospectroscopy using infrared photothermal nanospectroscopy (AFM-IR) technique. This technique overcomes the diffraction limit (of several microns) of conventional infrared microspectroscopy (μ-FTIR). The samples were mapped in the mid-IR range at a lateral spatial resolution about a hundred times better than with μ-FTIR. This provided us with unique in situ access to the distribution of the different infrared signatures of organic components at the sub-micron scale present in the Ryugu whole-rock samples as well as to the characterization of the compositional variability of Ryugu in the insoluble organic matter (IOM) chemically extracted from the Ryugu samples.

Methods. The AFM-IR maps of whole-rock particles and IOM residues from Ryugu samples were recorded with a lateral resolution of tens of nanometers. Spectra were recorded in the 1900–900 cm^{-1} spectral range by AFM-IR (Icon-IR) for all samples, and additional spectra were recorded from 2700 to 4000 cm^{-1} for one IOM sample by an optical photothermal IR (O-PTIR) technique using a mIRage® IR microscope.

Results. Organic matter is present in two forms in the whole-rock samples: as a diffuse phase intermixed with the phyllosilicate matrix and as individual organic nanoparticles. We identify the Ryugu organic nanoparticles as nanoglobule-like inclusions texturally resembling nanoglobules present in primitive meteorites. Using AFM-IR, we record for the first time the infrared spectra of Ryugu organic nanoparticles that clearly show enhanced carbonyl (C=O) and CH contributions with respect to the diffuse organic matter in Ryugu whole-rock and IOM residue.

Key words. methods: laboratory: solid state – techniques: imaging spectroscopy – interplanetary medium – meteorites, meteors, meteoroids – minor planets, asteroids: general

1. Introduction

The Hayabusa2 mission brought back well-preserved samples from the carbonaceous asteroid Ryugu. The Ryugu samples share strong similarities with CI chondrites (e.g., Yokoyama et al. 2023), which are meteorites with the most primitive chemical composition and a mineralogy that underwent a large extent of aqueous alteration (e.g., Brearley et al. 2006). Carbonaceous chondrites contain hydrated minerals and organic matter that may have contributed to the input of prebiotic matter on the early Earth (Pizzarello & Shock 2017). Investigating the organic matter of fresh carbonaceous asteroidal matter is of crucial importance to putting constraints on the formation of interplanetary organic matter and on the potential interaction between organic phases and the surrounding mineral matrix.

Vibrational spectroscopy is a powerful tool to elucidate the chemical structure of organic matter and minerals in meteorites and micrometeorites as well as in samples from the carbonaceous asteroid Ryugu (e.g., Dartois et al. 2018, 2023). The main limitation of classic infrared microspectroscopy (μ-FTIR) is diffraction, which limits the best achievable lateral resolution to a few microns, even with synchrotron techniques. To

overcome this diffraction limit, near-field infrared techniques such as scattering-type near-field scanning optical microscopy (s-SNOM; Dominguez et al. 2014; Yesiltas et al. 2021) and infrared photothermal nanospectroscopy (AFM-IR) can be used. The AFM-IR measurement is based on the detection of photothermal expansion of samples during IR absorption (Dazzi et al. 2005). This is an unparalleled technique to study the composition of organics and minerals at the nanoscale, and it is becoming more widely used to study the complexity of organic and mineral associations in meteoritic samples, as it gives direct access to the local IR signal (Mathurin et al. 2019; Kebukawa et al. 2019; Phan et al. 2022, 2023). Using a simple sample preparation that is compatible with infrared microscopy (μ-FTIR) and NanoSIMS, we recently achieved a multi-technique analysis of a fragment of a xenolithic clast from the Zag meteorite (Kebukawa et al. 2023a). The combination of techniques used in the analysis of the same sample allowed us to correlate isotopic compositions with chemical heterogeneities observed at the nanoscale. We previously reported the characterization of whole-rock Ryugu samples from chambers A and C with two different AFM-IR setups (see Yabuta et al. 2023). These first measurements gave insight into the organic matter distribution at the nanoscale, highlighting the presence of at least two main organic phases in Ryugu samples: a diffuse organic phase associated with the phyllosilicates and discrete organic patches showing different chemical compositions. In this study, we explore in detail the nanoscale repartition of organic matter in the sample as well as a possible relationship between components observed in the whole-rock and insoluble organic matter (IOM) Ryugu samples.

2. Samples and methods

The Ryugu samples analyzed in this work originate from chamber A (surface sample collected at the first touchdown site) and chamber C (potentially containing sub-surface material ejected from the Hayabusa2-made artificial crater) (Tachibana et al. 2022). An intact sample from Ryugu chamber A (A0108-19 whole-rock) as well as insoluble organic matter (IOM) extracted from chamber A and C samples were analyzed (A0106-IOM residue_3, and C0107-IOM residue_16-A and -B, respectively). These residues were prepared by HF/HCl demineralization at Hiroshima University from samples that had already been processed with solvent extraction with hexane, dichloromethane, methanol, hot water, formic acid, and HCl by the Soluble Organic Molecule (SOM) initial analysis team (Yabuta et al. 2023; Naraoka et al. 2023). Each fragment of the Ryugu "whole-rock" or IOM sample was micro-manipulated and transferred into a diamond compression cell made of two facing diamond windows. The fragments were flattened to a thickness of ~1 μm in order to provide an optimal thickness for infrared transmission microspectroscopy (μ-FTIR). After compression in the diamond cell, the flattened sample was generally distributed on each diamond window, providing two complementary flat samples named "top" and "bottom" depending on which diamond window the sample finally resides. In some cases, the majority of the sample remains on one diamond window only.

To measure IR maps at the tens of nanometer resolution, we used a technique combining an atomic force microscope (AFM) to a tunable IR laser, the AFM-IR. In these measurements, the AFM probe senses the photothermal expansion occurring in the sample induced after the infrared absorption of the material located under the AFM tip (Dazzi et al. 2005). In these conditions, the lateral resolution is no longer fixed by the diffraction limit, as in classical IR spectroscopy, but is related to the tip dimension, making it possible to achieve a tens of nanometers lateral resolution. The sensitivity of the technique is also improved compared to classical IR spectroscopy, as it was possible to achieve a molecular monolayer detection in the optimized mode (Lu et al. 2014). In this mode, called enhanced resonance mode, the maximal sensitivity was obtained by tuning the laser repetition rate to the value of an eigenmode of the cantilever. The position in frequency of the different eignemodes are mainly defined by the cantilever parameters. However, the mechanical properties of the sample beneath the tip can also induce a shift in frequency of the eigenmodes. On complex materials, such the ones that were observed here, the eigenmode maximal frequency is continuously tracked at the same time that the IR map is acquired. Consequently, the relative variation of local mechanical properties of the sample is simultaneously measured during IR map acquisition and can give indirect insight into the mechanical variation within the sample.

We note that since the AFM-IR technique relies on photothermal expansion, no signal should be detected when there is no infrared active mode in the sample. The AFM-IR system was an Icon-IR from Anasys Instrument (Bruker) coupled to a multi-chip quantum cascade laser (QCL; Daylight Solutions) covering the mid-IR range from 900 cm^{-1} up to 1960 cm^{-1} in four individual bands (1960–1706 cm^{-1}, 1706–1411 cm^{-1}, 1411–1209 cm^{-1} and 1209–900 cm^{-1}). The QCL power varies from one wavenumber to the other. To take these variations into account, a background was acquired on an external power meter, which was located at an equivalent optical path as the one from the QCL to the sample under the AFM tip. All the local spectra were divided by the acquired background. The IR mappings were also background corrected to take into account the difference in power from one wavenumber to the other. In this study, AFM-IR was used in contact mode with a gold-coated silicon AFM tip (Budget Sensors, ContGB-G, 13 kHz, 0.2 N m^{-1}). The IR mapping acquisitions were made using a 0.4 Hz scan rate with a laser power of around 5% for each QCL chip with a repetition rate of around 750 kHz and a pulse width of 100 ns. Infrared maps (images) were acquired at fixed laser wavenumbers: 1020 cm^{-1} (silicates); 1460 cm^{-1} (peak of CH_X); 1520 cm^{-1} (to estimate the local baseline for the CH_X due to other vibrational modes; see below); and 1720 cm^{-1} (C=O, chosen a few cm^{-1} higher than the carbonyl band maximum to avoid a residual C=C contribution). The signal at 1460 cm^{-1} represents the CH_X deformation modes' absorption with contributions from other vibrational modes. To highlight the CHX absorption, the absorption due to the continuum should be removed. Thus, the 1460 cm^{-1} images were subtracted from the 1520 cm^{-1} IR map (whole-rock Ryugu sample) or 1500 cm^{-1} IR map (IOM samples). The areas we studied using AFM-IR have already been analyzed using synchrotron FTIR microscopy (Dartois et al. 2023), and no carbonates have been observed, suggesting a lack of carbonate absorption in the 1400–1500 cm^{-1} spectral range. Each map acquisition consists of a topographic AFM image and an IR absorption map at the chosen wavenumber with a tens of nanometers lateral resolution. We took advantage of the intrinsically acquired topographic image to align the maps acquired at different wavenumbers. Final images were slightly smoothed using a 2-pixel kernel. The maps were combined in composite three color RGB (green, red, blue) images using several infrared vibrational groups of interest in order to better delineate the spatial variations at the tens of nanometer scale. To maximise the contrast in the composite image for bands with different intrinsic intensities, the intensity of each

image recorded at a given wavenumber was first normalized to its maximum intensity over the entire map before combining the images.

This article focuses on organic nanoparticles that were identified by the AFM-IR method. Individual lines of spectra covering the full QCL spectral range were acquired on some of the most remarkable regions identified in the images. The step size between each point was set to a few tens of nanometers (typically from 25 to 100 nm, depending on the acquisition). Intensity ratios of bands at frequencies corresponding to CH_X, C=C, and C=O were calculated from these spectra and are systematically shown as profiles in the figures showing the detailed analyses of the organic nanoparticles. These ratio profiles also give information on the dimension of the organic nanoparticles.

In addition to the AFM-IR measurement, chamber C Ryugu sample C0107-IOM residue_16-A was studied with an optical photothermal IR (O-PTIR) technique using a mIRage® infrared microscope (Photothermal Spectroscopy Corp., Santa Barbara, CA, USA). The physical concept of this technique is also to overcome the diffraction limit of the classical IR technique in order to achieve sub-micrometric lateral resolution by detecting photothermal expansion induced after the infrared absorption of the material. However, in the case of the mIRage® microscope, thermal expansion is detected using a 532 nm green laser instead of an AFM tip (for more details, see Zhang et al. 2016). In the setup used here, the illuminating laser is an OPO laser covering the spectral range from 2700 cm^{-1} to 4000 cm^{-1} and with a spectral resolution of around 8 cm^{-1}. The probe laser was a visible laser at 532 nm with the power set at 0.22%, acquired at a pulse rate of 100 kHz. The acquisition was made with a step size of 0.4 µm on a 27×27 grid (10.4 µm square grid), averaging two individual spectra for each recorded position. All the measurements were performed with a 40× objective (Schwarzschild, NA = 0.78).

3. Results

3.1. Ryugu 'whole-rock' sample

In Yabuta et al. (2023), we reported the analysis of Ryugu C whole-rock samples using AFM-IR in contact mode. It was then possible to highlight the heterogeneous distribution of organic matter in Ryugu samples. Some of the organic matter appeared rather homogeneously distributed in the phyllosilicate matrix, and individual particles were identified. To complete these first measurements, this present study focuses on analyses of whole-rock Ryugu samples from chamber A and IOM samples from chambers A and C. Figures 1 and 2 display the measurements performed on particle A0108-19 whole-rock. Figure 1a shows a large topographic image of the sample, while Figs. 1b through 1e were acquired on a zoomed-in region located at the top right of Fig. 1a (white box). Figure 1b displays the projected topographic image with a superimposed composite RGB image obtained by combining the IR maps obtained at different absorption bands: C=O at 1720 cm^{-1} (in red); C=C at 1600 cm^{-1} (in green); and the CH_X bonds (in blue), obtained subtracting the 1520 cm^{-1} IR map (which contains no specific absorption) from the 1460 cm^{-1} map (CH_X absorption) in order to take into account the continuum absorption. These three IR maps are shown individually in Figs. 1c through 1e. The RGB image (Fig. 1b) gives an insight into the organic matter distribution in the sample and also reveals the fine scale intrinsic heterogeneity of the organic matter. The main organic component appears in the form of a diffuse organic phase intimately mixed with the silicate component of Ryugu. This diffuse organic matter exhibits variations where the proportion of C=O, CH_X, and C=C differ from one area to another, as seen in the RGB maps encoding the different functional group variations in Fig. 2a and in Fig. 1b, where the RGB map is superimposed on the 3D topographic map of the sample. These variations can also be seen in the spectral profiles presented in Fig. 2b. The intensity of the CH_X deformation modes is always positive throughout the map (Fig. 1e), showing that CH_X modes contribute over the whole sample, with several small regions showing enhanced CH_X contributions. These results are in good agreement with the ones previously obtained for the Ryugu chamber C sample (Yabuta et al. 2023). In addition, a second organic matter component appeared in the sample studied as specific CH_X-rich hotspots (bright spot toward the top right of Fig. 1e). This bright hotspot in CH_X can also be clearly seen in the 3D image (Fig. 1b). The small spots visible in the same image appear less intense and could either be less enriched in CH_X or buried into the grain, thus contributing less to the AFM-IR signal.

This inclusion with a strong CH_X signal has a morphology resembling that of nanoglobules observed in other types of primitive meteorites (e.g., Garvie et al. 2008; Nakamura-Messenger et al. 2006; De Gregorio et al. 2013), in Stardust's samples from the comet 81P (Wild2) (De Gregorio et al. 2010, 2011), in IDPs and micrometeorites (Messenger et al. 2008; Maurette et al. 1995), and in other Ryugu samples (Daly et al. 2022; Yabuta et al. 2023; Stroud et al. 2022). Hereafter, the organic nanoparticles identified in this study are referred to as "nanoglobule-like" particles. Figure 2 represents a detailed analysis of the nanoglobule-like particle identified in Fig. 1e. Figure 2a displays a zoom-in of the RGB image on that particular feature; the nanoglobule-like particle is clearly visible close to the center of the analyzed area. It is surrounded by heterogeneous diffuse organic matter, as shown by different shades of red (C=O), green (C=C), and blue (CH_X). A line of spectra measured across the particle is shown as a white line. Figure 2b displays the variFation of the C=O/C=C (noted as 1700/1600) and CH_X/C=C (1460/1600) along the line profile. The location of the spectra (S_1 to S_3) presented in Fig. 2c is recalled on the left axis. Figure 2c displays typical AFM-IR spectra obtained along the line crossing the nanoglobule-like particle, with two typical spectra outside of the particle (S_1 and S_3, average spectra over the locations of the blue dots), and on the nanoglobule-like particle (S_2, average spectra over the location of the red dot). Spectra S_1 and S_3 correspond to matrix spectra. They exhibit a clear spectral contribution of phyllosilicates, the main mineral component, which has a strong band around and below 1100 cm^{-1}, and of the diffuse organic matter. This diffuse organic matter is characterized by the presence of the second most intense band, which is the C=C signature at 1600 cm^{-1}. The signature related to CH_X (1460 cm^{-1}) is weak but present. Small signatures were found at 1260 cm^{-1} and 1150 cm^{-1}, as already seen in some previous IR measurements of Ryugu samples (Yabuta et al. 2023; Dartois et al. 2023). The spectrum S_2 (in red in Fig. 2c), recorded at the position of the nanoglobule-like particle, substantially differs from its neighboring spectra S_1 and S_3. The intense band below 1100 cm^{-1} related to phyllosilicates is strongly reduced, confirming the ability of the AFM-IR technique to analyze small organic matter heterogeneities included in a complex matrix consisting of a mixture of organic matter and minerals. The S_2 spectrum revealed that, compared to the C=C feature, both the C=O and CH_X related features are significantly more intense in the nanoglobule-like particle than in the diffuse organic matter spectra S_1 and S_3.

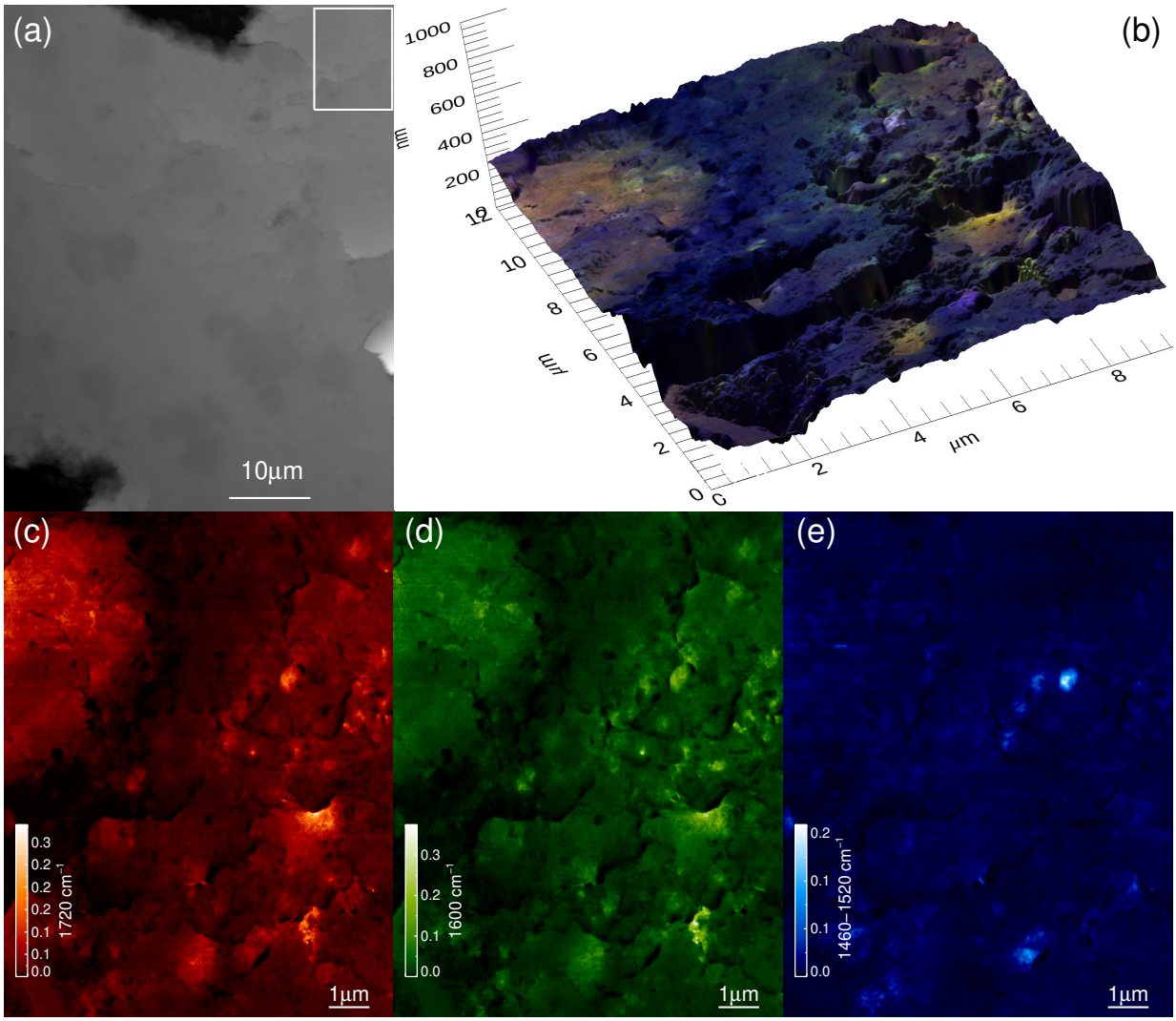

Fig. 1. AFM-IR maps of Ryugu A0108-19 whole-rock sample. (a) General large-scale topographic map of the grain. (b) Composite RGB maps (C=O in red, C=C in green, CH_X in blue) superimposed on the 3D topographic representation of the sample. (c-e) Individual maps in C=O (in red, at 1720 cm^{-1}), C=C (in green, at 1600 cm^{-1}), CH_X (in blue, peaked at 1460 cm^{-1}) used to build the composite RGB image. The CH_X deformation modes' map results from the subtraction of the 1520 cm^{-1} signal from the 1460 cm^{-1} signal, in order to suppress the contribution of other vibrational modes' absorption at 1460 cm^{-1} (see text for details).

These C=O and CH_X enhancements compared to C=C in the nanoglobule-like particle are illustrated in the profiles shown in Fig. 2b.

The spectrum labelled "Nanoglobule-like" in Fig. 2c (red dot-dashed line) was obtained by subtracting the contribution of the background matrix from spectrum S_2. This was achieved by subtracting from spectrum S_2 an average matrix spectrum as represented by S_1 and S_3, which was scaled to match the silicate signal of spectrum S_2. This spectrum shows a main C=O signature peaking around 1700 cm^{-1}, with a lower C=C than in the matrix and enhanced CH_X contributions with methylene and methyl deformation modes at ~1460 and ~1370 cm^{-1}. For the sake of comparison, a matrix spectrum corresponding to the thickness of the analyzed nanoglobule-like particle is presented as a dot-dashed blue line labelled "Matrix" in Fig. 2c. This spectrum is the average of S_1 and S_3 spectra, with a phyllosilicate signal normalized to that of the raw S_2 spectrum. The band intensity ratios between the "Nanoglobule-like" and "Matrix" signals are about four to five for the C=O and CH_X bands, and about two to three for the C=C band.

3.2. Insoluble organic matter analysis

Figures 3 to 8 display the AFM-IR studies on Ryugu IOM samples A0106-IOM residue_3 and C0107-IOM residue_16-A and -B. The presentation of the results follows the same layout as Figs. 1 and 2, with the first figures (Figs. 3, 5, and 7) displaying large topographic images of each sample on the diamond window with the region of interest (ROI) highlighted by a white box (top left) and the 3D topographic image with the superimposed RGB image (top right) made from individual IR maps of the ROI (bottom of figure) showing the repartition of C=O (in red, 1720 cm^{-1}), C=C (in green, 1600 cm^{-1}), and CH_X (in blue), which was obtained by subtraction of the 1500 cm^{-1} or 1520 cm^{-1} IR map (no specific absorption) from the 1460 cm^{-1} (CH_X absorption) map. Each ROI was chosen because of the presence of nanoglobule-like features both in topography and IR absorption maps. The additional figures for each sample (Figs. 4, 6, and 8) display a detailed study of the ROI with AFM-IR full span spectra along a line profile crossing the different identified nanoglobule-like structures. Two nanoglobule-like

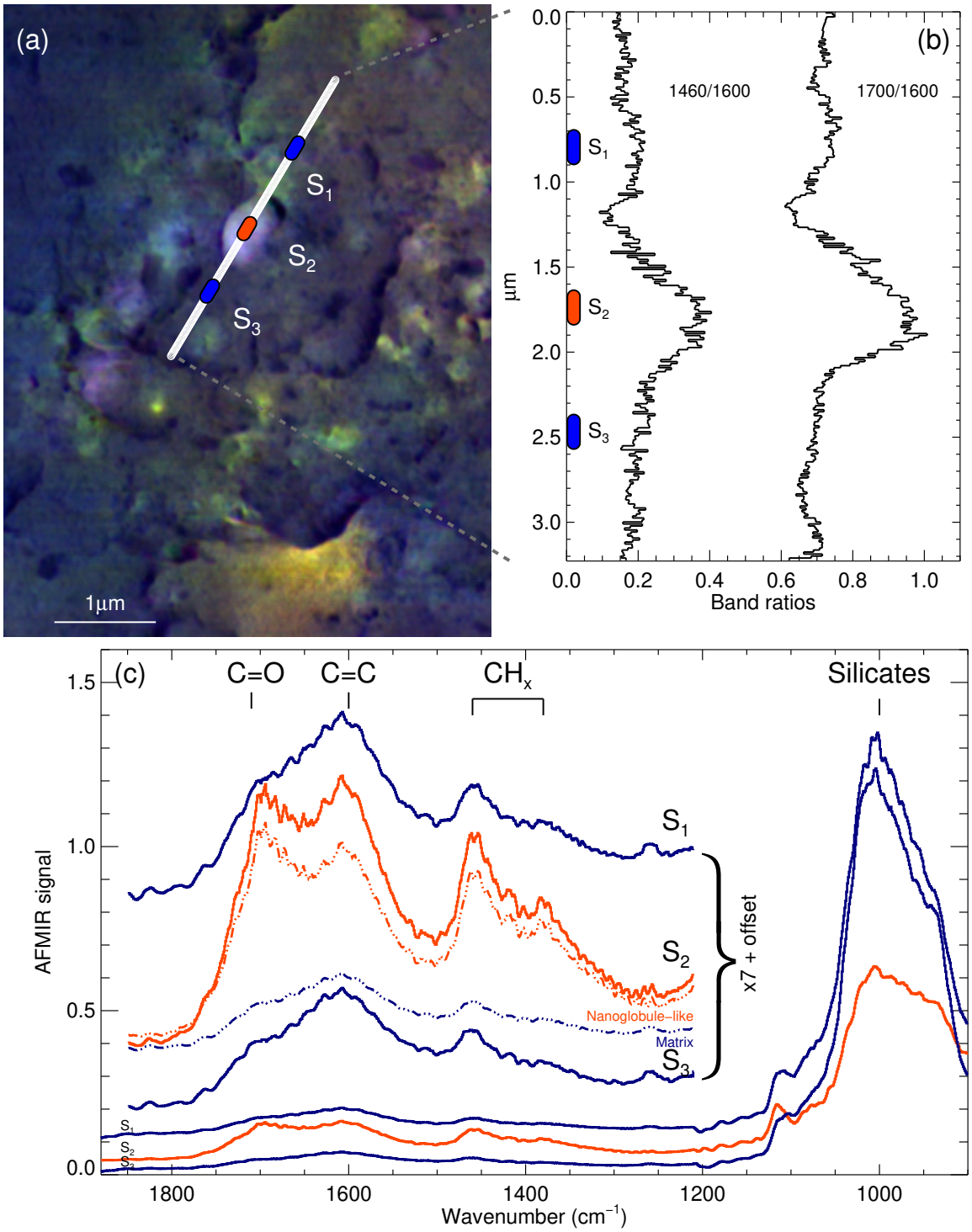

Fig. 2. Ryugu sample A0108-19 whole-rock, zoom-in on a region including the nanoglobule-like organic particle identified in situ in Fig. 1. (a) RGB image of the region including the organic nanoparticle (C=O at 1720 cm^{-1} in red, C=C at 1600 cm^{-1} in green, CH_X 1460 cm^{-1} minus 1520 cm^{-1} in blue). The white line shows the location of individual AFM-IR spectra taken across the nanoglobule-like feature. The colored dots (S_1 to S_3) correspond to average spectra taken on each side (S_1 and S_3 in blue) and on the nanoglobule-like feature (S_2 in red). (b) Intensity ratios of frequencies corresponding to CH_X/C=C (1460 cm^{-1}/1600 cm^{-1}) and C=O/C=C (1700 cm^{-1}/1600 cm^{-1}) along the white line shown in (a). The location of the S_1 to S_3 spectra is recalled on the left axis. (c) Average spectra on each side (blue, S_1, and S_3) and on the nanoglobule-like feature (red, S_2). The red dot-dashed line spectrum labelled "Nanoglobule-like" was obtained by scaling the average of S_1 and S_3 spectra to the same silicate band contribution, as in the S2 spectra, and by subtracting this scaled spectrum from S_2. The resulting "Nanoglobule-like" spectrum is thus freed from the matrix contribution underneath the globule. The nanoglobule-like spectrum shows an elevated CH_X signal (intense methyl and methylene deformation modes at ~1460 cm^{-1} and ~1370 cm^{-1}) as well as a high carbonyl contribution around 1700 cm^{-1}. The blue dot-dashed line spectrum labelled "Matrix" corresponds to the expected contribution from the matrix for a probe depth equivalent to the nanoglobule-like spectrum.

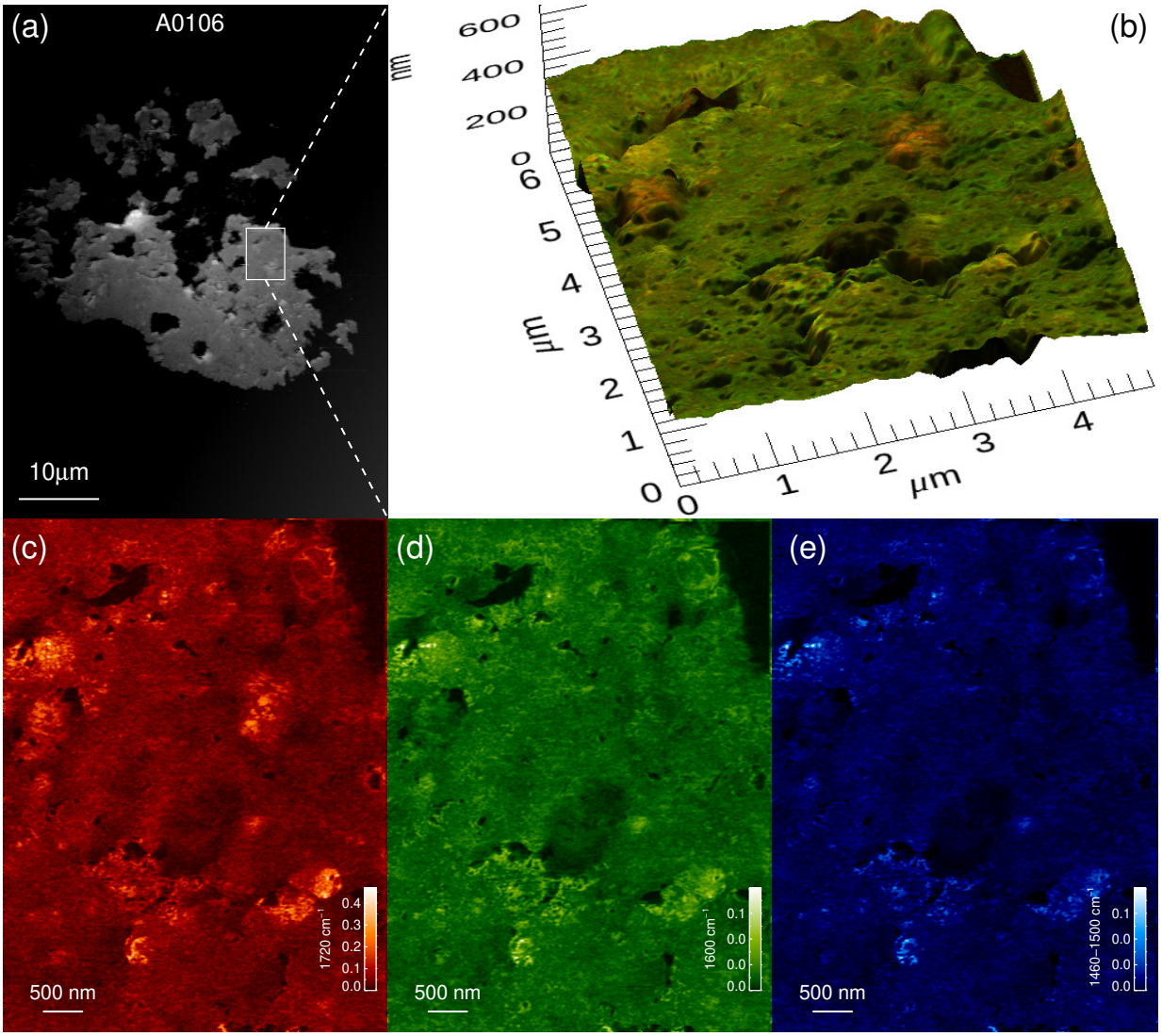

Fig. 3. AFM-IR maps of the Ryugu IOM A0106-IOM residue_3 sample. (a) General large-scale topographic map of the grain. (b) Composite RGB maps (C=O in red, C=C in green, CH_X in blue) superimposed onto the 3D topographic representation of the sample. (c–e) Individual maps in C=O (in red, at 1720 cm^{-1}), C=C (in green, at 1600 cm^{-1}), CH_X (in blue, peaked at 1460 cm^{-1}) used to build the composite RGB image. The CH_X deformation modes' map results from the subtraction of the 1520 cm^{-1} signal from the 1460 cm^{-1} signal, in order to suppress the contribution of other vibrational modes' absorption at 1460 cm^{-1} (see text for details).

structures are clearly visible from Ryugu sample A0106-IOM residue_3 (Fig. 3). Spectra extracted from a line profile in the upper-right nanoglobule-like particle displays enhanced C=O and CH_X relative absorption compared to that of C=C bonds (Fig. 4). Figures 5 and 7 display the studies of the two IOM samples from chamber C (C017-IOM residue_16-A and -B). The shapes of the nanoglobule-like particles from sample C0107-IOM residue_16-A (Figs. 5 and 6) consist of a double rounded structure with one larger structure with a diameter of 2–3 µm, which could contain several small nanoglobule-like particles, adjacent to a small structure with a diameter of about 1 µm. The two spectra extracted from the line on the larger structure (S_2 and S_3 in Figs. 6d-f) exhibit strong and well-defined features at 1720 cm^{-1} and 1460 cm^{-1}, indicating that the contribution of both C=O and CH_X relative to that of C=C is much stronger in the nanoglobule-like particle than in the rest of the IOM (see Figs. 6d-f). The results obtained here are in rather good agreement with those for the whole-rock analysis, but careful analysis of the spectra obtained on the IOM nanoglobule-like particles showed a significant absorption band at 1680 cm^{-1} that is less visible in the whole-rock nanoglobule-like particle spectra. The intensity of this band varies among the nanoglobule-like particles, and it is larger in sample A0106-IOM residue_3 (spectrum S_2 in Fig. 4) than in C0107-IOM residue_16-A (spectra S_2 and S_3 in Fig. 6) and C0107-IOM residue_16-B (spectra S_2 to S_4 in Fig. 8). The feature centered at 1680 cm^{-1} is associated with a C=O signature and more specifically favors the presence of carboxylic acid over ketone and/or esters (for characteristic band positions, see, e.g., Bellamy 1975a,b,c).

To complete the AFM-IR analysis, the sample C0107-IOM residue_16-A was studied with an O-PTIR technique (Figs. 6a–c). Compared to AFM-IR, the expected lateral resolution achievable here is one to two orders of magnitude lower, but it allows for the analysis of an area slightly greater than that studied with classical AFM-IR. Furthermore, with the system used here, the spectral range from 2700 cm^{-1} to 4000 cm^{-1}

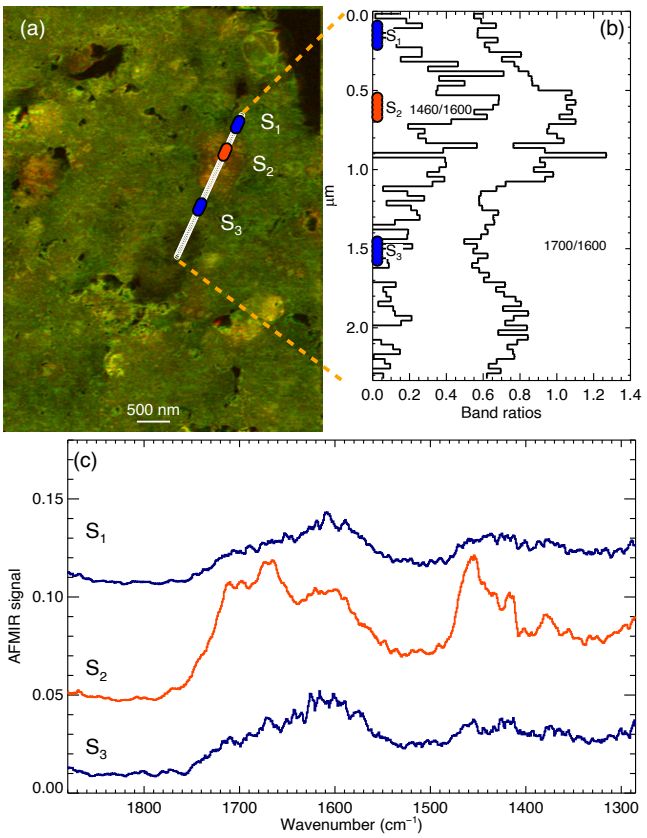

Fig. 4. AFM-IR characterization of the Ryugu IOM A0106-IOM residue_3, zoom-in on the organic nanoparticles identified in situ in Fig. 3. (a) RGB image of the region including the organic nanoparticles (C=O at 1720 cm^{-1} in red, C=C at 1600 cm^{-1} in green, CH_X 1460 cm^{-1} minus 1520 cm^{-1}) in blue. The white line shows the location of individual AFM-IR spectra taken across one organic nanoparticle. The colored dots (S_1 to S_3) correspond to the average spectra taken on each side (S_1 and S_3 in blue) and on the organic nanoparticle (S_2 in red). (b) Intensity ratios of frequencies corresponding to CH_X/C=C (1460/1600) and C=O/C=C (1700/1600) along the white line shown in (a). The location of the S_1 to S_3 spectra is recalled on the left axis. (c) Average AFM-IR spectra on each side (blue, S_1 and S_3) and on the organic nanoparticle (red, S_2).

is complementary to that of the AFM-IR analysis used in this study. Figure 6b shows the optical image of the sample C0107-IOM residue_16-A. This optical image was compared with the topographic AFM image in order to colocalize the acquisitions from the two techniques. Figure 6a represents a projected IR map extracted from a hyper-spectral acquisition (step size 500 nm) by integrating the CH_X stretching mode IR absorption band. On this map, it is clearly possible to recognize the round shape of the nanoglobule-like particle cluster previously observed in AFM-IR (Figs. 5 and 6d-f). Comparison between the spectra obtained in the cluster and in the matrix (Fig. 6c) showed a higher absorption in the CH_X region as well as a very broad OH stretching mode absorption showing an asymmetric spectroscopic profile extending up to 3500 cm^{-1}, which is compatible with the presence of alcohol and the carboxylic acid -OH functional group seen in organic residues (Muñoz Caro & Schutte 2003; Modica et al. 2012; Zhu et al. 2020). In combination with the measured 1680 cm^{-1} carbonyl contribution, the presence of carboxylic acid is likely.

The nanoglobule-like particle observed in the second IOM sample from chamber C (C0107-IOM residue_16-B) is slightly more elongated in shape (see Fig. 7b). The three AFM-IR point spectra measured along this nanoglobule-like particle (S_2, S_3 and S_4, Fig. 8c) are very similar to the ones from the previous nanoglobule-like particles from chambers A and C. Again, the relative contribution of both C=O and CH_X lines are stronger in the nanoglobule-like particle compared to the surrounding material (Fig. 8, spectra S_1 and S_5), where the contribution of C=C dominates.

From a general point of view, the relative intensities of C=O, C=C, and CH_X in the two IOM samples from chamber C are similar to those observed in the IOM sample from chamber A. A detailed study reported for the three IOM samples (Figs. 4, 6, and 8) confirmed that the average spectra of the nanoglobule-like areas (spectra S_2 in Fig. 4; S_2 and S_3 in Fig. 6; and S_2, S_3, and S_4 in Fig. 8) exhibit a stronger C=O and CH_X signal than the surrounding diffuse organic matter (spectra S_1 and S_3 in Fig. 4; S_1 and S_4 in Fig. 6; and S_1 and S_5 in Fig. 8).

4. Discussion

4.1. Diffuse organics in Ryugu whole-rock and insoluble organic matter samples

The diffuse organic matter of Ryugu shows a significant polyaromatic composition with the predominance of a C=C signature and lower contributions of C=O and CH_X, as seen in Figs. 2, 4, 6, and 8. This signature is compatible with the observation of Yabuta et al. (2023) that the diffuse organic matter of Ryugu is comparable to IOM extracted from carbonaceous chondrites, although STXM-XANES analyses also identified a molecular carbonate signature in the diffuse Ryugu organic matter. The latter component is no longer present after the IOM extraction process. The AFM-IR spectral signatures of this diffuse organic matter in Ryugu is qualitatively similar in the whole-rock samples and in the extracted IOM (see spectra in Figs. 2, 4, and 6), but relative abundances vary. Based on a comparison between the composite RGB figures obtained from the whole-rock Ryugu chamber A sample (Fig. 9a) and from Ryugu chambers A and C IOM samples (Figs. 9b-d), it appears that the contribution of CH_X (in blue) relative to C=C (in red) is higher in the whole-rock sample than in the IOM samples. We also observed this in the spectra in the whole-rock sample (S_1 and S_3 in Fig. 2) and in the IOM (e.g., S_1 and S_5 in Fig. 8, where the CH_X signature is the lowest). By comparison, the CH_X signal in the spectra from the IOM nanoglobule-like particles remained equivalent to what was observed in the whole-rock spectra, showing that the CH_X were not degraded during the IOM production process. However, the increase of the C=O absorption band at 1680 cm^{-1} in the IOM compared to the whole-rock samples may indicate a change in the chemical composition of the nanoglobule-like particle that could result from the acid etching that was applied to the samples to recover the IOM. As a consequence, the main hypothesis to explain the decrease of the CH_X signal in the IOM sample is that this signature is associated with labile organic species that are removed during the procedure of acid etching of Ryugu samples in order to extract the IOM. This result is in agreement with Kebukawa et al. (2019), who also observed that aliphatic-rich organics were missing in the IOM obtained after demineralization of carbonaceous chondrites. Looking at the distribution of the diffuse organic matter in the whole-rock sample, the CH_X signature of these labile molecules seems intimately linked to the phyllosilicates. Viennet et al. (2023) have suggested that organics are contained in the interlayer space of Ryugu smectites, whereas the interlayer space of Orgueil

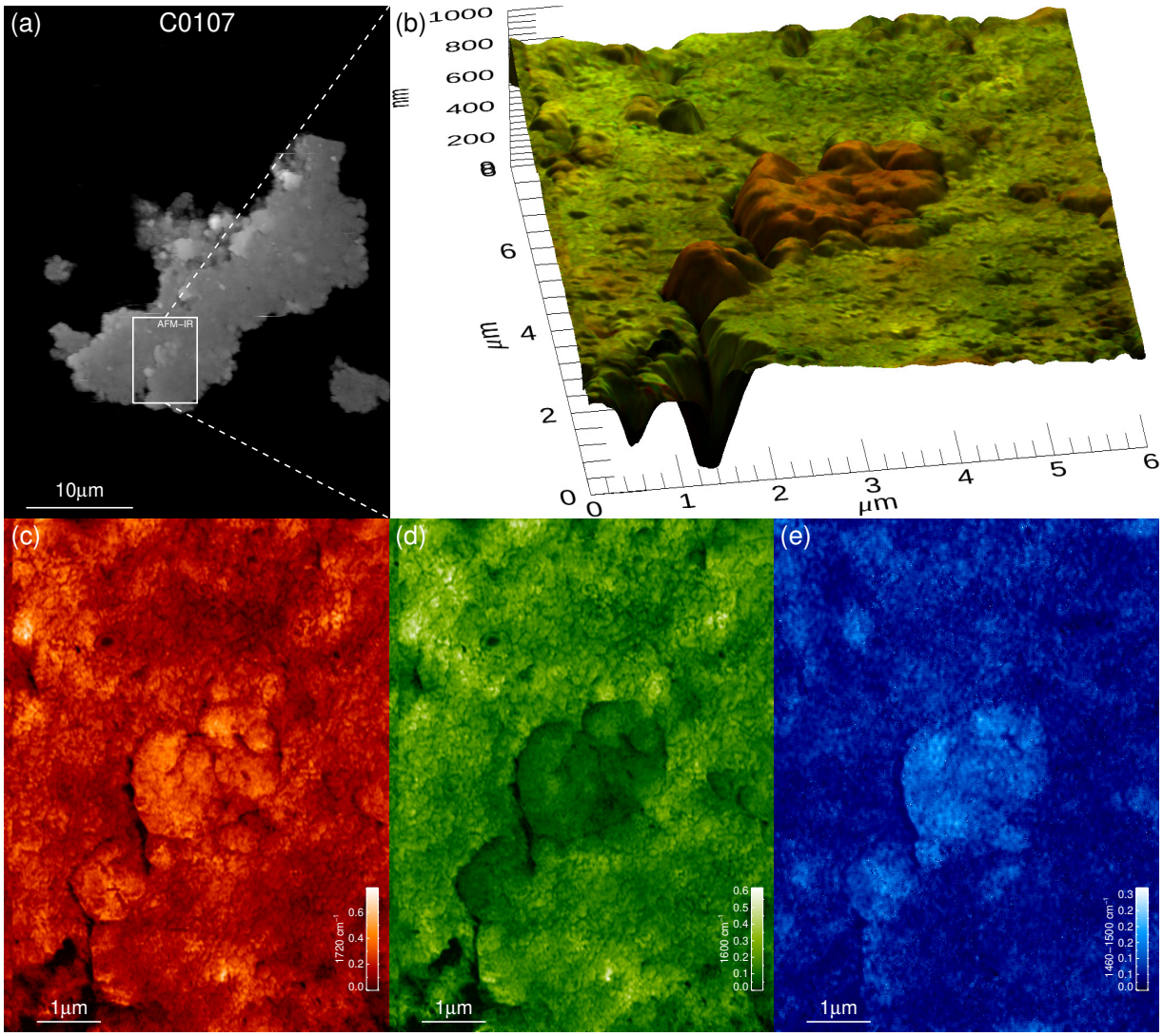

Fig. 5. AFM-IR maps of the Ryugu IOM C0107-IOM residue_16-A sample. (a) General large-scale topographic map of the grain. (b) Composite RGB C=O, C=C, CH_X map superimposed on the 3D topographic representation of the sample. (c-e) Individual C=O (in red, at 1720 cm^{-1}), C=C (in green, at 1600 cm^{-1}), CH_X (in blue, peaked at 1460 cm^{-1}) images used to build the composite RGB image. The CH_X deformation modes' map results from the subtraction of the 1500 cm^{-1} signal from the 1460 cm^{-1} signal, in order to suppress the contribution of other vibrational modes' absorption at 1460 cm^{-1} (see text for details).

only contains water. The presence of these organic molecules, possibly rich in N-H, could be responsible for the signatures around 3.1 µm (3.06 and 3.24 µm, or 3270 and 3090 cm^{-1}) observed on raw samples by Pilorget et al. (2022); Yada et al. (2022) and in IOM samples by Kebukawa et al. (2023b). Future IR nanospectroscopy of Ryugu samples with a larger analytical wavelength range would be required to assess whether the labile component observed here is rich in N-H.

4.2. Nanoglobule(-like) particles in whole-rock and insoluble organic matter Ryugu samples

4.2.1. In situ infrared spectra of an individual nanoglobule-like particle in a whole-rock Ryugu sample

The AFM-IR technique allows for the analysis of nanoglobule-like particles in situ in the silicate matrix without the chemical extraction needed to obtain the IOM. The IR signature of an individual Ryugu nanoglobule-like particle can be obtained in this study from the whole-rock measurements after considering the probing depth of the AFM-IR technique, and it would represent the first IR measurement of a nanoglobule(-like) particle. The lateral resolution of AFM-IR in the experimental condition used in this study is around 50 nm, but the depth of integration can reach a few micrometers, depending on the analytical conditions and on the material analyzed. In this work, it means that the obtained signal in the spectra is integrated from the whole thickness of the sample, as the sample's thickness varies from around 500 nm (IOM samples) to 1 µm (whole-rock sample). The penetration depth is related to the propagation of the photothermal signal, which is detected by the AFM tip and depends on different factors that are related to both the experimental conditions (such as the repetition rate of the laser) and the nature of the sample as it depends on the thermal and mechanical properties of its different components. Studies that have focused on the evaluation of the sample's probing depth have always used polymeric model samples (Quaroni 2020; Mathurin et al. 2022). The samples studied here are a mixture

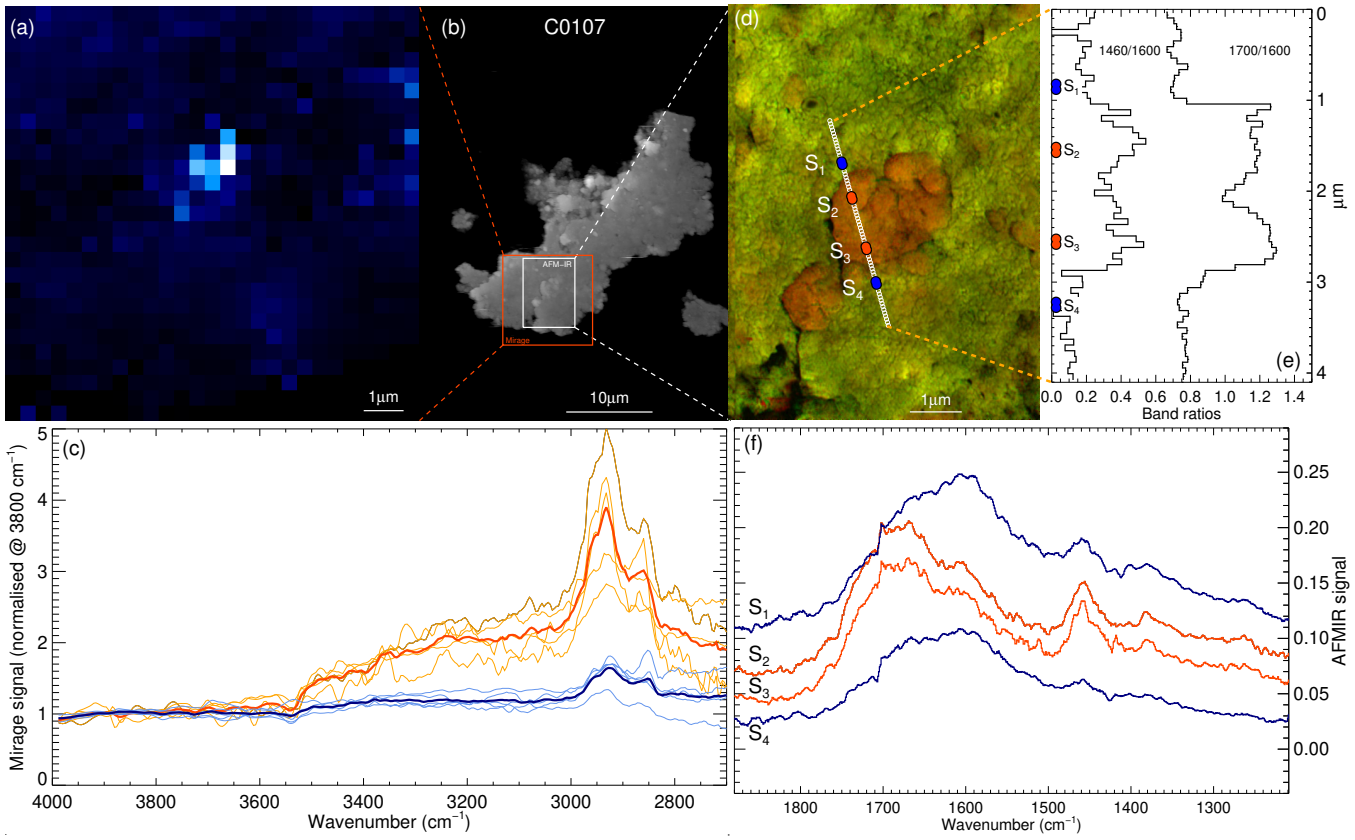

Fig. 6. Ryugu IOM sample C0107-IOM residue_16-A. Zoom-in on a region including the organic nanoparticle assemblage identified in situ in Fig. 5. These organic nanoparticles were both analyzed with the O-PTIR technique using a mIRage® and with AFM-IR. (a) Projected IR map integrating the CH_X stretching mode absorption band over the 3050–2750 cm^{-1} range from the mIRage® analysis (lateral resolution of 500 nm). (b) Large-scale topographic map of the grain and the location of the analyses by O-PTIR (red box corresponding to the map in (a)) and AFM-IR (white box corresponding to the maps shown in (d). (c) Spectra from the hyperspectral mapping over the organic nanoparticle region using O-PTIR. Individual spectra on the organic nanoparticles (in red) show a higher absorption in the CH_X region (average spectra in bold curve). The blue spectra are from the neighboring areas and show lower CH_X absorption (average spectrum in bold blue curve). (d) RGB image of the region including the nanoglobule (C=O at 1720 cm^{-1} in red, C=C at 1600 cm^{-1} in green, CH_X 1460 cm^{-1} minus 1520 cm^{-1} in blue). The white line shows the location of individual AFM-IR spectra taken across the nanoglobule assemblage. The colored dots (S_1 to S_4) correspond to average spectra taken on each side (S_1 and S_4 in blue) and on the organic nanoparticles (S_2 and S_3 in red). (e) Intensity ratios of frequencies corresponding to CH_X/C=C (1460/1600) and C=O/C=C (1700/1600) along the white line shown in (d). The location of the S_1 to S_4 spectra is recalled on the left axis. (f) Average AFM-IR spectra on each side (blue, S_1 and S_4) and on the organic nanoparticles (red, S_2 and S_3).

of inorganic phases (dominated by phyllosilicates) and organic phases, with different mechanical and thermal properties, which makes it impossible to model the complete behavior of the bulk sample. However, it is still possible to obtain an approximate probing depth value using the experimental results. By focusing on the nanoglobule-like particle identified in the Ryugu sample A0108-19 whole-rock (Figs. 1 and 2), it appears that the intensity of the phyllosilicate band around 1000 cm^{-1} is significantly lower in the spectra taken from the nanoglobule-like particle by more than a factor of two (Fig. 2c). The nanoglobule-like particle lateral size is on the order of 500 nm, as shown in the AFM-IR maps and in the spectral profile, showing the CH_X (at 1460 cm^{-1}) to silicate intensity ratio in the whole-rock sample (Fig. 2b). From the AFM probing in contact mode, it is possible to gain insight on the mechanical properties of the samples. The analyses of the nanoglobule-like particle in the Ryugu sample A0108-19 whole-rock do not show large deviations of the nanoglobule's mechanical properties compared to that of the surrounding matrix. This was also observed for the other nanoglobule-like particles in this study, suggesting either that these particles are not hollow or that they contain a mineral core, similar to what was observed by Hashiguchi et al. (2013).

The analysis of the obtained AFM-IR signal also gives an insight on the structure of the nanoglobule. In AFM-IR analysis, the observed signal is integrated along the thickness, and as a consequence, the signal of a shell of a core-shell structure appears as a circle around the core, as seen in Mathurin et al. (2018). In the case of the nanoglobule-like particle analyzed in this work, the signal appears homogeneously distributed, which is not compatible with a hollow particle or a mineral-bearing nanogblobule. Assuming a spherical shape of the nanoglobule-like particle, we derived that the probing depth is on the order of twice the size of the particle, that is, about 1 µm. This becomes an upper limit of the probing depth if there is a silicate core in the nanoglobule-like particle that can contribute to the silicate band around 1000 cm^{-1}. As a consequence, the spectra obtained from the nanoglobule-like particle correspond to a mixture of the real particle's signature and the matrix beneath it (diffuse organic matter and phyllosilicate). If we assume that the diffuse organic matter signal is directly proportional to that of the phyllosilicate, it is possible to retrieve the signature of the nanoglobule-like particle by subtracting the surrounding organic matter-diffuse signature from that of the nanoglobule-like particle, after normalization of the spectra to the height of

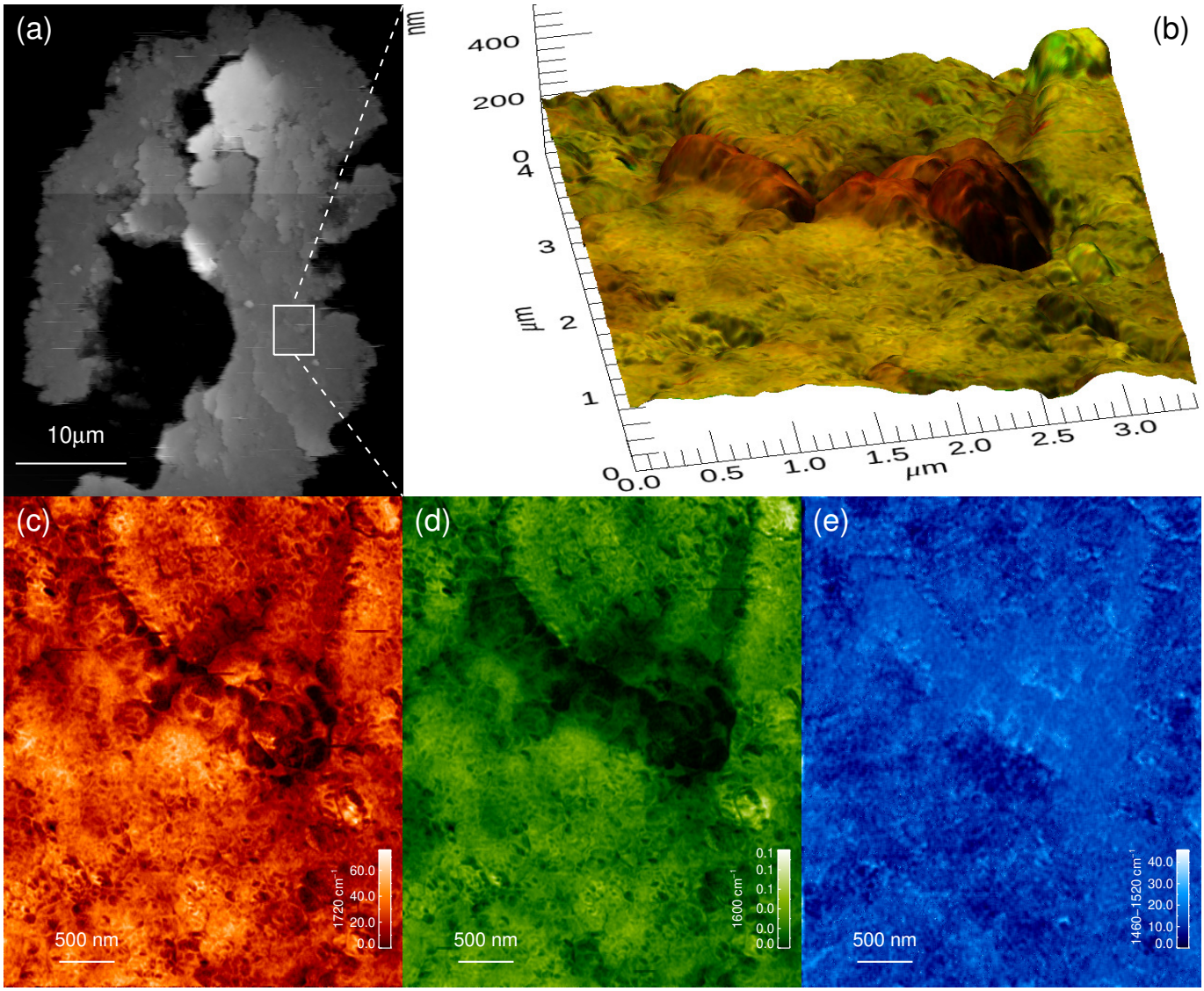

Fig. 7. AFM-IR maps of the Ryugu IOM sample C0107-IOM residue_16-B. (a) General large-scale topographic map of the grain. (b) Composite RGB C=O, C=C, CH_X map superimposed on the 3D topographic representation of the sample. (c–e) Individual C=O (in red, at 1720 cm^{-1}), C=C (in green, at 1600 cm^{-1}), CH_X (in blue, peaked at 1460 cm^{-1}) images used to build the composite RGB image. The CH_X deformation modes' map results from the subtraction of the 1520 cm^{-1} signal from the 1460 cm^{-1} signal in order to suppress the contribution of other vibrational modes' absorption at 1460 cm^{-1} (see text for details).

the phyllosilicate band. The result of this subtraction is given in Fig. 2c (spectrum S_2 "Nanoglobule-like," red dot-dashed line). This proposed nanoglobule-like IR signature shows a polyaromatic composition but contains less C=C and is significantly enriched in C=O and CH_X compared to the diffuse organic matter component and the IOM of Ryugu. A more precise analysis of the C=O signature in the nanoglobule-like particle revealed two sub-bands, with one centered around 1680 cm^{-1} and the other centered around 1720 cm^{-1}, which may indicate the presence of carboxylic acid and ketone chemical functions in the nanoglobule-like particle, respectively.

4.2.2. Spectroscopic signatures of nanoglobules and nanoglobule-like particles in Ryugu

Nanoglobules were identified, both solid and hollow, isolated and in clusters, with diameters typically less than 400 nm. A few individual organic nanoparticles exhibited diameters as large as 2 µm. In STXM-XANES analyses of Ryugu FIB sections, Yabuta et al. (2023) reported the presence of IOM-like nanoglobules and identified highly aromatic nanoglobules as well as aromatic nanoglobules that show a composition with a large and narrow C=C peak, little or no C=O, and a peak due to C–C and carboxyl O=C-OH functions at 288–289 eV. Daly et al. (2022) reported that the outer surface of a nanoglobule in Ryugu samples contains phyllosilicate crystals that are growing into their surfaces. Mappings by EELS has shown that nanoglobules are layered, with each layer showing a different amount of carbon. The inner layers contain less carbon and oxygen than the outer layers. Nitrogen is sometimes detected inside a nanoglobule.

The nanoglobule-like particles in Ruygu from this AFM-IR study show large C=O and CH_X signatures associated with a smaller aromatic carbon (C=C) contribution than in the surrounding matrix. The composition of the nanoglobule-like particles identified in this study are very rich in CH_X,

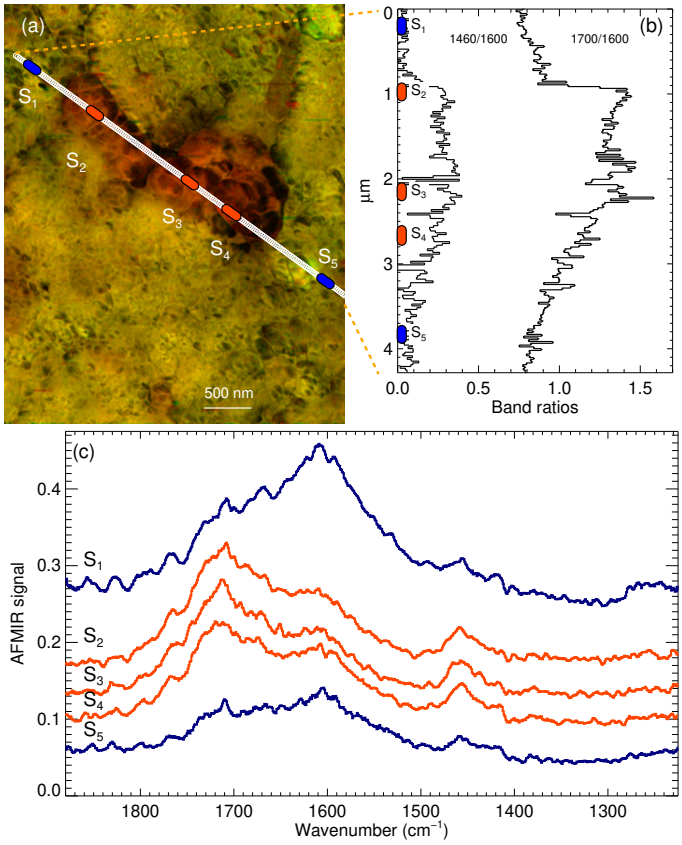

Fig. 8. Ryugu IOM sample C0107-IOM residue_16-B. Zoom-in on the organic nanoparticles identified in situ in Fig. 7. (a) RGB image of the region including the organic nanoparticles (C=O at 1720 cm^{-1} in red, C=C at 1600 cm^{-1} in green, CH_X 1460 cm^{-1} minus 1520 cm^{-1} in blue). The white line shows the location of individual AFM-IR spectra taken across the organic nanoparticles. The colored dots (S_1 to S_5) correspond to average spectra taken on each side (S_1 and S_5 in blue) and on the organic nanoparticles (S_2 to S_4 in red). (b) Intensity ratios of frequencies corresponding to CH_X/C=C (1460/1600) and C=O/C=C (1700/1600) along the white line shown in (a). The location of the S_1 to S_5 spectra is recalled on the left axis. (c) Average AFM-IR spectra on each side (blue, S_1 and S_5) and on the organic nanoparticle (red, S_2 to S_4).

which are functional groups that are not usually interpreted in STXM-XANES spectra, as their signatures are not easily seen unless they are very abundant. The CH_X enrichment observed in the nanoglobule-like particles' composition by AFM-IR is not biased by the analytical technique since the IR illumination of the sample does not have an effect on the organic matter composition. Nuevo et al. (2011), in contrast, observed a transformation of aliphatic carbon into aromatic carbon in the produced organic residues due to interaction with the X-ray beam during STXM-XANES analyses for dwell times larger than 1–2 ms. This highlights the advantage of analyzing samples by AFM-IR with a well-controlled laser power density, although meteoritic organics did not show evidence of irradiation damage during STXM-XANES analyses (De Gregorio et al. 2013). We did not identify IOM-like or "highly aromatic" organic nanoparticles in our Ryugu samples. This could result from a statistical bias, as an IOM-like globule was identified by Phan et al. (2023) in another Ryugu sample. The observed lack of highly aromatic nanoglobule-like particles in our Ryugu samples is however compatible with the decrease of the abundance of this type of nanoglobule with increasing aqueous alteration in carbonaceous chondrites, as seen in De Gregorio et al. (2013). Moreover, although only three organic nanoparticle aggregates were found in our IOM sampling, they all show the same characteristic spectral signatures (Figs. 4c, 6c, 8c). These signatures bear similarities with those of the nanoglobule-like particle in the whole-rock sample, except for a slightly stronger C=O and a weaker C=C absorption (Fig. 2c). This could be an effect of the acid etching to recover the IOM, stressing the importance of measuring the compositions in situ without chemical treatments.

From a morphological point of view, some changes were also observed between the nanoglobule-like particles from the whole-rock and IOM samples we studied. In the whole-rock sample, the nanoglobule-like particle appears isolated in the silicate matrix, with an average diameter of around 500 nm. In IOM samples, especially in the case of chamber C samples, it is possible to distinguish several nanoglobule-like particles that appear to have aggregated as assemblages of a few microns in size (see Fig. 9). This may imply that during the IOM production process of our samples, a physicochemical phenomenon occurred that led to the concentration of the different nanoglobule-like particles from the whole-rock samples into assemblages. Consequently, a few of the advantages of direct analysis of whole-rock samples using the AFM-IR technique is the possibility to analyze nanoglobule-like particles in an isolated state as well as keeping the information on the mineralogical surroundings and chemical context.

4.3. Ryugu nanoglobule-like particles compared to their meteoritic counterparts

Nanoglobules were first identified in Orgueil and Ivuna and proposed as indigenous microfossils (Claus & Nagy 1961). They were then rediscovered by Nakamura et al. (2002) and Garvie & Buseck (2006), who dismissed the idea of these structures being of biogenic origin. Nanoglobules are present in primitive meteorites (e.g., De Gregorio et al. 2013), in Stardust's samples returned from the comet 81P (Wild2) (De Gregorio et al. 2010), in micrometeorites (Maurette et al. 1995), UCAMMs (Bradley & Ishii 2017; Yabuta et al. 2017), and in chondritic anhydrous IDPs and micrometeorites (Messenger et al. 2008; Bradley et al. 2022; Noguchi et al. 2022).

In meteorites, nanoglobules typically range in size from less than 200 nm to an upper limit of about 1 to 2 µm (e.g., Nakamura et al. 2002; Garvie & Buseck 2004; Floss & Stadermann 2009; Herd et al. 2011; De Gregorio et al. 2013; Changela 2015) They can occur as isolated structures in the matrix or in clusters (e.g., Garvie et al. 2008). The average size of the nanoglobules tends to increase with the level of aqueous alteration of the meteorites (De Gregorio et al. 2013), suggesting that all nanoglobules may be sensitive to aqueous alteration.

Microspectroscopy techniques, mainly EELS and STXM-XANES, have been used to measure the composition of nanoglobules found in primitive meteorites and Stardust's samples (e.g., De Gregorio et al. 2010, 2013). Two main chemical compositions of nanoglobules have been defined. Firstly, the main population is "IOM-like" and contains aromatic C=C, carbonyl, and carboxylic functional groups (a subpopulation contains clear ^{15}N enrichments compared to IOM). The second composition comprises highly aromatic nanoglobules with high a proportion of C=C and very low or no aromatic ketone (C=O) signatures. Most of these nanoglobules are hollow and show ^{15}N enrichments, compared to IOM and to the main population of IOM-like nanoglobules that are not ^{15}N rich. In De Gregorio et al. (2013), the fraction of highly aromatic

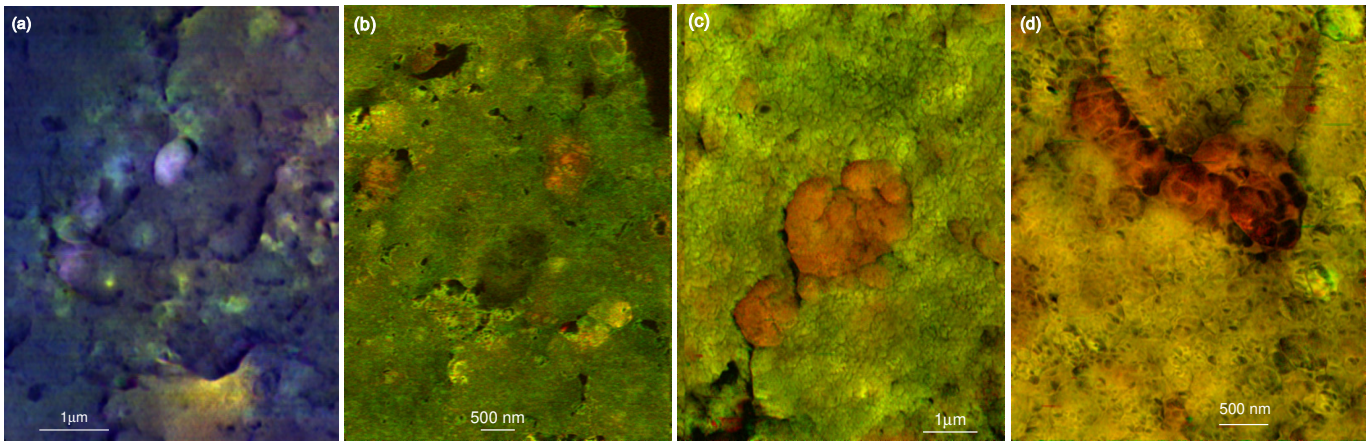

Fig. 9. Overview of the composite RGB images of the carbonaceous inclusions (organic nanoparticles) in Ryugu samples: (a) A0108-19 whole-rock; (b) A0106-IOM residue_3; (c and d) C0107-IOM residue_16-A and -B. In red, C=O (1720 cm^{-1}); in green, C=C (1600 cm^{-1}); in blue, CH_X (peaked at 1460 cm^{-1}). The CH_X deformation modes' map results from the subtraction of the 1520 cm^{-1} signal from the 1460 cm^{-1} signal, in order to suppress the contribution of other vibrational modes' absorption at 1460 cm^{-1} (see text for details).

nanoglobules seemed to decrease when parent body aqueous alteration increased (no nanoglobule of this kind was found in Orgueil), but Herd et al. (2011) found the opposite trend when studying several lithologies of Tagish lake with increasing degrees of hydrothermal alteration.

The compositions of nanoglobule-like particles in Ryugu from this AFM-IR study appear to be similar in surface (chamber A) and subsurface (chamber C) sampling, indicating their ubiquitous presence within in-depth Ryugu material. In the Ryugu nanoglobule-like particles identified in this study, the substructure of the C=O peak around 1700 cm^{-1} as well as the band observed around 3500 cm^{-1} by the mIRage® instrument are compatible with a significant abundance of carboxylic (R-COOH) functional group in the nanoglobule-like particles. This composition is marginally in agreement with the aromatic nanoglobule family but with less aromatic C=C than in the STXM-XANES analyses of Ryugu nanoglobules in Yabuta et al. (2023).

Formation mechanisms proposed for the nanoglobules mainly include (1) a pre-accretionary scenario by UV (or ion irradiation) processing of organic-rich ices around minerals (or plain ices) with diverse evolutionary processes on the parent body (e.g., Nakamura-Messenger et al. 2006; Dworkin et al. 2001; Hashiguchi et al. 2013) or (2) a parent body formation by chemical reactions during aqueous alteration on the parent body, possibly by a reaction between formaldehyde and glycoaldehyde undergoing formose reaction (Cody et al. 2011; Kebukawa et al. 2013). In meteorites, nanoglobules are usually D and ^{15}N rich (e.g., De Gregorio et al. 2013), suggesting formation in a cold environment, either in the protosolar cloud or in the external regions of the protoplanetary disk, before incorporation in the parent body. Hashiguchi et al. (2013) observed nanoglobules containing minerals, but these minerals did not show O isotopic anomalies, suggesting that they are not of presolar origin. The authors therefore favored the formation of the nanoglobules in the protoplanetary disk. Muñoz Caro & Schutte (2003) and Nuevo et al. (2011) experimentally simulated the physical conditions present in dense clouds prior to the protostellar collapse, which are also relevant conditions for the densest phases of the protoplanetary disk, and the accretion and photoprocessing of ices on grain surfaces. Among the different compositions of ice analogues investigated, some spectra of the

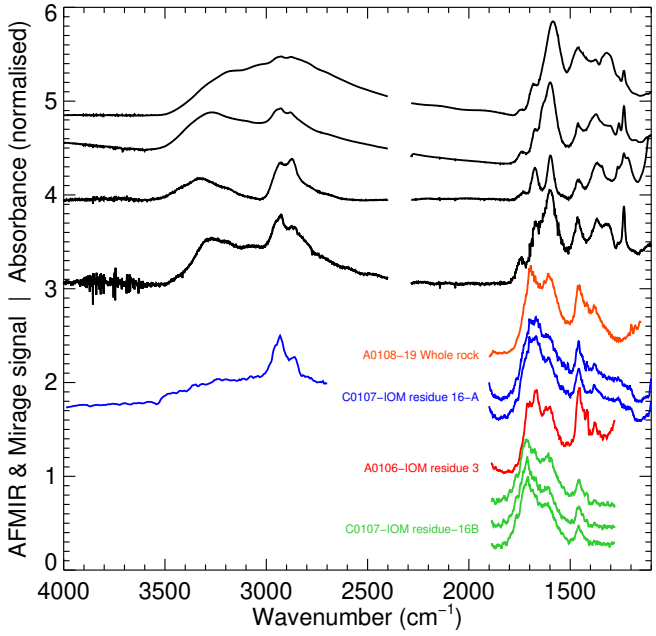

Fig. 10. Comparison of AFM-IR and O-PTIR (mIRage®) spectra of nanoglobule-like inclusions from this study with IR spectra of some macromolecular residues from Muñoz Caro & Schutte (2003), obtained after irradiation of interstellar ice analogues and annealing to room temperature. These irradiation experiments simulate the physical conditions in dense clouds and the accretion and photoprocessing of ices on grain surfaces.

macromolecular residue remaining after the irradiation process and containing the refractory products of the photo and thermal processing presented infrared characteristics similar to that of the nanoglobule-like particles analyzed in this study (Fig. 10). The composition of the nanoglobule-like particles enriched in C=O and CH_X, as measured in this study, are compatible with a formation by ion or UV irradiation, as shown in these experiments.

4.4. Conclusions

We used infrared nanospectroscopy (AFM-IR and O-PTIR) to characterize the infrared signatures of organic matter in Ryugu

samples returned by the Hayabusa2 mission. The AFM-IR technique overcomes the diffraction limit of conventional IR microscopy, with spectroscopic maps and spectra that can be recorded with a lateral resolution of about 50 nm. Two main organic phases were found in the Ryugu samples: a diffuse organic component intimately mixed with the mineral matrix and nanoglobule-like organic particles. Complementary to our work reported in Yabuta et al. (2023), this article reports a detailed analysis of several nanoglobule-like particles identified in both whole-rock and IOM samples from the surface (chamber A) and sub-surface (chamber C) of Ryugu. We identify these nanoglobule-like particles with the nanoglobules found in primitive meteorites, micrometeorites, IDPs, and 81P (Wild2) samples. In Ryugu samples, nanoglobules are one of the two most abundant organic microstructures (Daly et al. 2022; Yabuta et al. 2023; Stroud et al. 2022). In this study, we found that some of the Ryugu nanoglobules are agglomerated in the IOM after chemical extraction.

This work provides the first individual IR spectral signatures of several nanoglobule-like particles from the Ryugu carbonaceous asteroid, and it shows that they have an IR signature significantly different from that of the main diffuse organic matter in Ryugu. The key characteristic of all nanoglobule-like particles observed in both whole-rock and IOM extracts is being substantially enriched in both carbonyl (C=O) and CH_X and having a lower abundance of aromatic carbon (C=C) compared to the main diffuse organic component. The nanoglobule-like particle IR signatures appear to be similar in surface (chamber A) and sub-surface (chamber C) sampling, indicating their ubiquitous presence within in-depth Ryugu material. The IR signatures of the nanoglobule-like particles are fairly similar in the whole-rock and IOM samples, with some changes in the C=O speciation, possibly due to the IOM extraction procedure. The IR signature of the nanoglobule-like particles is compatible with UV or ion irradiation of ices in the outer regions of the protoplanetary disk or in the protosolar cloud.

This study also provides insight for future AFM-IR analyses. To retrieve only the IR signature of nanoglobule-like particles, we showed that it is necessary to control the probing depth so that it is smaller than the thickness of the nanoglobule-like particles. This may be achieved by changing the AFM-IR setup used for the measurement, for instance, by performing the experiment in tapping mode instead of contact mode and using the surface-sensitive mode currently in development (Mathurin et al. 2022). Working on a thinner sample preparation (such as FIB sections, as proposed by Phan et al. 2022) could also be a possibility. Further constraints on the formation process of the nanoglobule-like particles can be placed by coupling these AFM-IR analyses with the measurement of their isotopic compositions using the NanoSIMS technique at the same spatial resolution (e.g., Rojas et al. 2020; Kebukawa et al. 2023b).

Acknowledgements. The Hayabusa2 spacecraft was developed and built under the leadership of JAXA, with contributions from the German Aerospace Center (DLR) and the Centre National d'Études Spatiales (CNES) and in collaboration with NASA; Nagoya University; University of Tokyo; National Astronomical Observatory of Japan (NAOJ); University of Aizu; Kobe University; and other universities, institutes, and companies in Japan. We thank the many engineers, including N. Inaba at JAXA and T. Masuda, S. Yasuda, K. Matsushima, and T. Ohshima at NEC Corporation for their dedicated work on the Hayabusa2 mission. Part of the equipment used in this work has been funded by the French INSU-CNRS program "Physique et Chimie du Milieu Interstellaire" (PCMI). This work was also supported in France by the Centre National d'Etudes Spatiales (CNES, MIAMI-H2 project), by region Ile de France (DIM-ACAV+, C3E and SACHEM projects; DIM-MAP, MUSIICS project), by the LabEx P2IO, by Agence Nationale de la Recherche (ANR) (COMETOR ANR-18-CE31-0011), and by PEPR ORIGINS France 2030 (ANR-22-EXOR-0007 axis "Chemical and isotopic analysis of primitive extraterrestrial materials"). The authors would like to thank G.M. Caro for fruitful exchanges that added scientific value to the content of the paper, as well as for the molecular residue data in Fig. 10 that allowed comparison with the Ryugu data.

References

Bellamy, L. J. 1975a, Aldehydes and Ketones (Dordrecht: Springer Netherlands), 149
Bellamy, L. J. 1975b, Carboxylic Acids (Dordrecht: Springer Netherlands), 183
Bellamy, L. J. 1975c, Esters and Lactones (Dordrecht: Springer Netherlands), 203
Bradley, J. P., & Ishii, H. 2017, MAPS, 52 A33
Bradley, J. P., Ishii, H. A., Bustillo, K., et al. 2022, Geochim. Cosmochim. Acta, 335, 323
Brearley, A. J., Binzel, R. P., Walker, R. M., & Cameron, A. G. W. 2006, in Meteorites and the Early Solar System II, ed.s D. S. Lauretta, & H. Y. McSween (University of Arizona Press), 587
Changela, H. G. 2015, Geochim. Cosmochim. Acta, 159, 285
Claus, G., & Nagy, B. 1961, Nature, 192, 594
Cody, G. D., Heying, E., Alexander, C. M. O., et al. 2011, PNAS, 108, 19171
Daly, L., Lee, M. R., Bland, P. A., et al. 2022, in LPI Contributions, 2678, 53rd Lunar and Planetary Science Conference, 2258
Dartois, E., Engrand, C., Duprat, J., et al. 2018, A&A, 609, A65
Dartois, E., Kebukawa, Y., Yabuta, H., et al. 2023, A&A, 671, A2
Dazzi, A., Prazeres, R., Glotin, F., & Ortega, J. M. 2005, Opt. Lett., 30, 2388
De Gregorio, B. T., Stroud, R. M., Nittler, L. R., et al. 2010, Geochim. Cosmochim. Acta, 74, 4454
De Gregorio, B. T., Stroud, R. M., Cody, G. D., et al. 2011, Meteor. Planet. Sci., 46, 1376
De Gregorio, B. T., Stroud, R. M., Nittler, L. R., et al. 2013, Meteor. Planet. Sci., 48, 904
Dominguez, G., Mcleod, A. S., Gainsforth, Z., et al. 2014, Nat. Commun., 5, 5445
Dworkin, J. P., Deamer, D. W., Sandford, S. A., & Allamandola, L. J. 2001, PNAS, 98, 815
Floss, C., & Stadermann, F. J. 2009, ApJ, 697, 1242
Garvie, L. A., & Buseck, P. R. 2004, Earth Planet. Sci. Lett., 224, 431
Garvie, L. A. J. & Buseck, P. R. 2006, Meteor. Planet. Sci., 41, 633
Garvie, L., Baumgardner, G., & Buseck, P. R. 2008, Meteor. Planet. Sci., 43, 899
Hashiguchi, M., Kobayashi, S., & Yurimoto, H. 2013, Geochim. Cosmochim. Acta, 122, 306
Herd, C. D. K., Blinova, A., Simkus, D. N., et al. 2011, Science, 332, 1304
Kebukawa, Y., Kilcoyne, A. L. D., & Cody, G. D. 2013, ApJ, 771, 19
Kebukawa, Y., Alexander, C. M. O., & Cody, G. D. 2019, Meteor. Planet. Sci., 54, 1632
Kebukawa, Y., Mathurin, J., Dartois, E., et al. 2023a, Icarus, 400, 115582
Kebukawa, Y., Quirico, E., Dartois, E., et al. 2023b, Meteor. Planet. Sci., submitted
Lu, F., Jin, M., & Belkin, M. A. 2014, Nat. Photonics, 8, 307
Mathurin, J., Pancani, E., Deniset-Besseau, A., et al. 2018, The Analyst, 143, 5940
Mathurin, J., Dartois, E., Pino, T., et al. 2019, A&A, 622, A160
Mathurin, J., Dartois, E., Dazzi, A., et al. 2022, 53rd Lunar and Planetary Science Conference, 2678, 2142
Maurette, M., Engrand, C., Brack, A., et al. 1995, Lunar and Planetary Science Conference, XXVI, 913
Messenger, S., Nakamura-Messenger, K., & Keller, L. P. 2008, in Lunar and Planetary Science Conference, 2391
Modica, P., De Marcellus, P., Baklouti, D., et al. 2012, Eur. Astron. Soc. Publ. Ser., 58, 343
Muñoz Caro, G. M., & Schutte, W. A. 2003, A&A, 412, 121
Nakamura, K., Zolensky, M. E., Tomita, S., Nakashima, S., & Tomeoka, K. 2002, Int. J. Astrobiol., 1, 179
Nakamura-Messenger, K., Messenger, S., Keller, L. P., Clemett, S. J., & Zolensky, M. E. 2006, Science, 314, 1439
Naraoka, H., Takano, Y., Dworkin, J. P., et al. 2023, Science, 379, eabn9033
Noguchi, T., Matsumoto, R., Yabuta, H., et al. 2022, Meteor. Planet. Sci., 57, 2042
Nuevo, M., Milam, S. N., Sandford, S. A., et al. 2011, Adv. Space Res., 48, 1126
Phan, V. T. H., Rebois, R., Beck, P., et al. 2022, Meteor. Planet. Sci., 57, 3
Phan, V. T. H., Beck, P., Rebois, R., et al. 2023, Meteor. Planet. Sci., 57, 1
Pilorget, C., Okada, T., Hamm, V., et al. 2022, Nat. Astron., 6, 221
Pizzarello, S., & Shock, E. 2017, Origins Life Evol. Biospheres, 47, 249
Quaroni, L. 2020, Analyt. Chem., 92, 3544
Rojas, J., Duprat, J., Nittler, L. R., et al. 2020, 51st Lunar and Planetary Science Conference, held 16-20 March, 2020 at The Woodlands, Texas, LPI Contribution No. 2326, 1614

Stroud, R. M., De Gregorio, B. T., Burgess, K. D., et al. 2022, LPI Contributions, 2695, 6064
Tachibana, S., Sawada, H., Okazaki, R., et al. 2022, Science, 375, 1011
Viennet, J. C., Roskosz, M., Nakamura, T., et al. 2023, Geochem. Perspect. Lett., 25, 8
Yabuta, H., Noguchi, T., Itoh, S., et al. 2017, Geochim. Cosmochim. Acta, 214, 172
Yabuta, H., Cody, G. D., Engrand, C., et al. 2023, Science, 379, eabn9057
Yada, T., Abe, M., Okada, T., et al. 2022, Nat. Astron., 6, 214
Yesiltas, M., Glotch, T. D., & Kaya, M. 2021, ACS Earth Space Chem., 5, 3281
Yokoyama, T., Nagashima, K., Nakai, I., et al. 2023, Science, 379, abn7850
Zhang, D., Li, C., Zhang, C., et al. 2016, Sci. Adv., 2, 1
Zhu, C., Turner, A. M., Meinert, C., & Kaiser, R. I. 2020, ApJ, 889, 134

[1] Institut Chimie Physique, UMR8000, Univ. Paris-Saclay, CNRS, 91405 Orsay, France
e-mail: jeremie.mathurin@universite-paris-saclay.fr
[2] Laboratoire de Physique des deux infinis Irène Joliot Curie, UMR 9012, Univ. Paris-Saclay, CNRS, 91405 Orsay, France
[3] Institut des Sciences Moléculaires d'Orsay, UMR8214, CNRS, Univ. Paris-Saclay, 91405 Orsay, France
[4] Institut de Minéralogie, Physique des Matériaux et de Cosmochimie, Museum National d'Histoire Naturelle, CNRS, Sorbonne Université, 75231 Paris, France
[5] Department of Earth and Planetary Sciences, Tokyo Institute of Technology, Tokyo 152-8551, Japan
[6] Department of Earth and Planetary Systems Science, Hiroshima University, Higashi-Hiroshima, Hiroshima 739-8526, Japan
[7] Institut de Planétologie et d'Astrophysique, Université Grenoble Alpes, 38000 Grenoble, France
[8] Synchrotron SOLEIL, CNRS, CEA, Paris-Saclay, 91190, Saint-Aubin, France
[9] Earth and Planets Laboratory, Carnegie Institution of Washington, 5241 Broad Branch Road NW, Washington, DC 20015, USA
[10] Materials Science and Technology Division, US Naval Research Laboratory, Washington, DC 20375, USA
[11] Graduate School of Environmental Studies, Nagoya University, Chikusa-ku, Nagoya 464-8601, Japan
[12] Advanced Light Source, Lawrence Berkeley National Laboratory, Berkeley, CA 94720-8229, USA
[13] The Graduate University for Advanced Studies, SOKENDAI, Hayama, Kanagawa 240-0193, Japan
[14] Department of Earth Sciences, Waseda University, Shinjuku-ku, Tokyo 169-8050, Japan
[15] Centro de Química Estrutural, Institute of Molecular Sciences and Department of Chemical Engineering, Instituto Superior Técnico, Universidade de Lisboa, Av. Rovisco Pais 1, 1049-001 Lisboa, Portugal
[16] Department of Earth Sciences, Tohoku University, Sendai 980-8578, Japan
[17] École normale supérieure de Lyon, Université de Lyon, 69342 Lyon, France
[18] Institute for Molecular Science, UVSOR Synchrotron Facility, Myodaiji, Okazaki 444-8585, Japan
[19] Department of Earth and Planetary Science, The University of Tokyo, Bunkyo-ku, Tokyo 113-0033, Japan
[20] NASA Ames Research Center, Moffett Field, CA 94035-1000, USA
[21] Materials Science and Technology Division, US Naval Research Laboratory, Washington, DC 20375, USA
[22] Spectroscopy Division, Japan Synchrotron Radiation Research Institute JASRI), Sayo-gun, Hyogo 679-5198, Japan
[23] Institute of Materials Structure Science, High Energy Accelerator Research Organization, KEK, Tsukuba, Ibaraki 305-0801, Japan
[24] Research and Utilization Division, Japan Synchrotron Radiation Research Institute (JASRI), Sayo-gun, Hyogo 679-5198, Japan
[25] Division of Earth and Planetary Sciences, Kyoto University, Kitashirakawa Oiwakecho, Sakyo-ku, Kyoto 606-8502, Japan
[26] Department of Earth and Planetary Sciences, Kyushu University, Fukuoka 819-0395, Japan
[27] Institute of Space and Astronautical Science, Japan Aerospace Exploration Agency, Sagamihara 252-5210, Japan
[28] Department of Natural History Sciences, Hokkaido University, Sapporo 060-0810, Japan
[29] Isotope Imaging Laboratory, Creative Research Institution, Hokkaido University, Sapporo 001-0021, Japan
[30] Kanagawa Institute of Technology, Atsugi 243-0292, Japan
[31] Department of Earth and Planetary Sciences, Nagoya University, Nagoya 464-8601, Japan